Internal wave generation in the presence of a turning depth

Allison Lee, Julie Crockett
Department of Mechanical Engineering
Brigham Young University

Abstract

Internal waves are formed in stably stratified fluids where the natural frequency (N) of the fluid is greater than the excitation frequency (ω). If $N < \omega$, only evanescent waves form. Evanescent waves, which decay at an exponential rate, can become propagating internal waves if N increases above ω. Experiments were performed to investigate the effects of topography shape, distance between the topography and the turning depth (where $N = \omega$), and the strength of the stratification as measured by the Froude number in both the evanescent and propagating regions. It was found that internal waves with the highest kinetic energy were generated by the medium Gaussian and that decreasing the distance between topography and the turning depth increased the kinetic energy over the entire range of tested values and topographical shapes. However, Fr_{evan} was a strong influence on kinetic energy for only a portion of the tested values.

1 Introduction

A stratified fluid is one where the density of the fluid varies based on the height of the fluid. The ocean and atmosphere are both examples of stratified fluids. In the ocean, the increasing salinity and the decreasing temperature leads to increased density with depth. In the atmosphere, the decreasing temperature with increasing height causes the change in density. A stratified fluid is defined by the natural frequency, (N) which is calculated with

$$N^2 = \frac{-g}{\rho_o}\frac{d\rho}{dz} \tag{1}$$

Here, g is the gravity constant, ρ_o is a reference density, and $d\rho/dz$ is the change of density with respect to height. As the change in density increases, N increases, and is referred to as a strong stratification, while a weak stratification indicates small changes of density with height.

Because of the stratification of the atmosphere and ocean, both fluids are capable of sustaining internal waves [1, 2]. Internal waves are generated from a disturbance in the stratified fluid. One example of this is the tides moving over oceanic topography. The M2 semi-diurnal tide is a well known generator of internal waves [3]. As the M2 tide oscillates over underwater topography, internal waves are generated. Internal waves propagate away from their generation sites and have an important impact on oceanic circulation and mixing [1, 2]. Because of this, it is important to understand where internal waves are generated and factors that will affect the energy within internal waves.

Internal waves can only be formed if the natural frequency of the stratified fluid is greater than an excitation frequency (ω) of a disturbance (such as the tides), i.e. $N > \omega$.

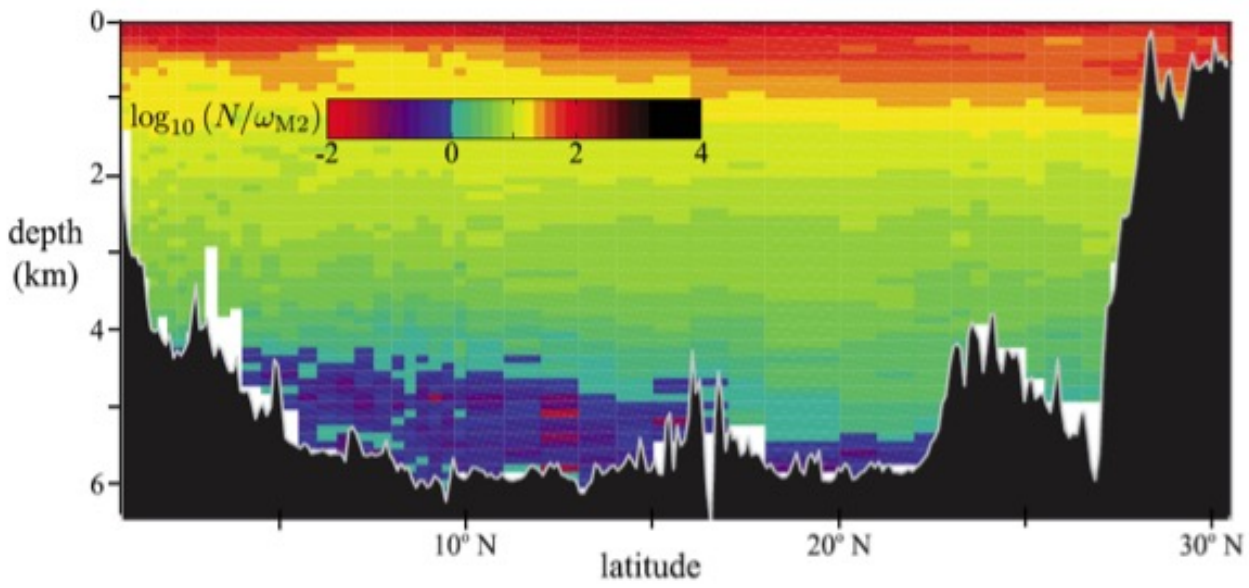

Figure 1: A comparison of the natural frequency of the Philippine Sea to the M2 tidal frequency. Evanescent regions occur where $\log(N/\omega_{M2}) < 0$, and propagating regions where $\log(N/\omega_{M2}) > 0$. Figure created by [4].

If $N < \omega$, then the bulk fluid cannot react to the excitation frequency and only evanescent waves are generated. While internal waves suffer little to no viscous dissipation, the amplitudes of evanescent waves begin to decay immediately after forming [5]. It has often been assumed that evanescent waves have a negligible effect in stratified fluids because of their decaying properties, but linear theory shows that evanescent waves can become propagating internal waves [1]. If the stratified fluid has a varying natural frequency, then the there could be both an evanescent region ($N < \omega$) and a propagating region ($N > \omega$) present in the same fluid. King et al. calculated the natural frequency of the ocean in many different locations and compared N to ω_{M2} [3]. Paoletti et al. plotted an example of this data in shown in Figure 1 [4]. The colors correspond to the logarithmic ratio of N/ω_{M2}. An evanescent region occurs where $\log(N/\omega_{M2}) < 0$, while the propagating region are indicated by a ratio greater than 0. Because of the varying natural frequency, it is possible for the M2 tide to generate both evanescent and internal waves. Paoletti et al. used numerical simulations and experiments to show that evanescent waves could be generated, move towards a turning depth (where $\omega = N$), and then become an internal wave once the wave passes into a propagating region. While these internal waves generated from evanescent waves have less energy (due to the dissipation of the evanescent waves), they could still have in important impact on the surrounding ocean. This paper uses experiments to explore the effects of topography shape and relative distance to the turning depth on the kinetic energy of internal waves generated from evanescent waves passing through a turning depth.

2 Experimental Methods

All experiments were performed in an acrylic tank with a length, width and height of 2.45m, 0.15m, and 0.91m respectively. A modified version of the double bucket method

[6] was used to create an exponential density profile. Density measurements using an Anton Par density meter were taken every 2cm before the first set of data was taken, and then every 5 cm after every fourth experimental run. The density measurements were fit to the equation

$$\rho = a\exp(bz) + c \tag{2}$$

where ρ and z have units of kg/m^3 and m, and a, b, and c are coefficients calculated from the fit. This density profile ensures a varying N profile for every experiment, with N ranging from $0.3 - 2.0s^{-1}$. Along the top of the tank, a track with a stepper motor controls the oscillation frequency and excursion length of the topography which generates waves. As shown in Figure 2, the topography is inverted, with lower values of N at the base of the topography. Moving away from the topography and towards the bottom of the tank, z decrease while density and N increase.

Two different topographies were used in the experiments. Both were Gaussian shaped curves of the form

$$h = H\exp(-x^2/B^2) \tag{3}$$

where H is the peak height of the topography and $B^2 = 18W^2$. Here, W is the width of the topography when the height of the topography has decayed to 1% of the maximum height H. Two separate topographies were used. The first is defined by $H = 0.1$m and $W/H = 1.45$, and is referred to as the Medium Gaussian. The second has $H = 0.11$m and $W/H = 0.45$, and is called the Steep Gaussian.

The frequency of the topography oscillation was chosen based off of the desired location of the turning depth (z_{td}), which is calculated from the natural frequency profile $N(z_{td}) = \omega$. The height of the turning depth also influences the value of H/D, where D is the distance from the turning depth to the top of the topography. Table 1 outlines the various experimental cases, including the topography used, the coefficients for the density profile (2), the oscillation frequency (ω), and H/D, and the total water height (z_{total}). Also listed are Fr_{evan} and Fr_{prop}. The Froude number is the ratio of $Fr = \omega/N$. Because N varies with height, Fr will change throughout the experimental tank, and so average values of N in each region were used to calculate an average Fr. This allows for a comparison of the effects of the natural frequency on wave kinetic energy.

Synthetic Schlieren was used to calculate variations in density for each experiment

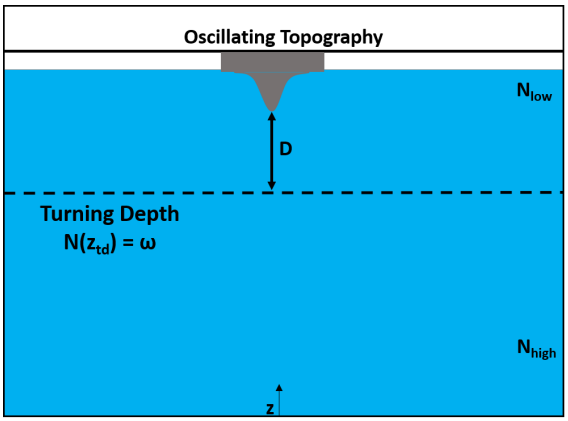

(a) Experimental Setup

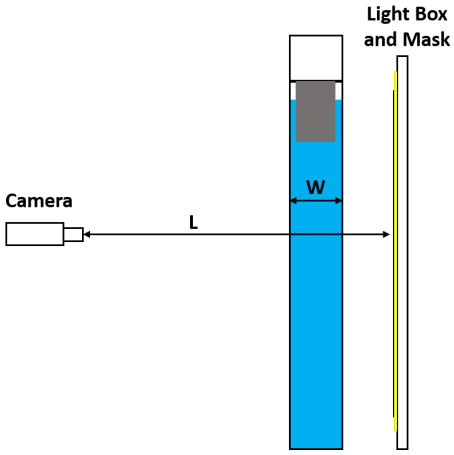

(b) Synthetic Schlieren Setup

Figure 2: A front (2a) and side (2b) view of the experimental tank.

Table 1: A summary of experiments and experimental parameters. Values of a, b, and c are used in Eq. 2, ω is the frequency of the topography oscillation, H/D is the ratio of the height of the topography to the distance from the tip of the topography to the turning depth, and Fr_{evan} and Fr_{prop} are the average Froude numbers in their respective regions.

Case	a	b	c	Water Height (m)	Topography	ω	z_{td}	H/D	Fr_{evan}	Fr_{prop}
1	100.41	-2.36	992.75	0.605	Medium	1.03	0.32	0.70	1.17	0.82
2	97.67	-2.35	994.17	0.630	Medium	0.99	0.34	0.83	1.17	0.80
3	95.16	-2.55	997.64	0.636	Medium	0.94	0.34	0.83	1.17	0.80
4	110.42	-1.35	974.60	0.729	Medium	0.94	0.35	0.48	1.13	0.88
5	101.58	-1.51	983.59	0.712	Medium	1.04	0.41	0.28	1.20	0.91
6	106.61	-1.39	978.11	0.686	Medium	0.90	0.41	0.72	1.09	0.86
7	89.84	-2.17	998.60	0.651	Medium	0.84	0.42	1.28	1.11	0.77
8	84.88	-2.48	1004.92	0.617	Medium	0.84	0.42	0.94	1.12	0.75
9	92.56	-2.39	996.75	0.605	Medium	0.85	0.45	1.78	1.09	0.75
10	86.93	-2.81	1004.45	0.605	Medium	0.80	0.46	2.12	1.10	0.70
11	92.56	-2.39	996.75	0.591	Medium	0.93	0.38	1.33	1.13	0.78
12	95.21	-2.64	1002.57	0.581	Medium	1.20	0.19	0.31	1.27	0.87
13	95.21	-2.64	1002.57	0.545	Medium	1.08	0.28	0.42	1.18	0.82
14	118.87	-1.87	981.55	0.484	Medium	1.12	0.28	0.40	1.09	0.87
15	127.28	-1.48	967.40	0.508	Medium	1.20	0.16	0.36	1.13	0.94
16	116.81	-1.76	980.83	0.547	Medium	0.99	0.40	0.76	1.06	0.83
17	95.31	-3.37	1012.53	0.511	Medium	0.99	0.24	1.90	1.15	0.73
18	88.82	-3.71	1008.09	0.627	Steep	1.03	0.29	0.37	1.34	0.74
19	87.77	-3.50	1006.67	0.667	Steep	1.23	0.19	0.27	1.47	0.83
20	87.77	-3.50	1006.67	0.609	Steep	1.16	0.22	0.43	1.37	0.81
21	92.17	-4.01	1010.61	0.565	Steep	0.96	0.34	0.68	1.24	0.69
22	94.71	-4.49	1013.92	0.592	Steep	0.81	0.41	1.11	1.21	0.60
23	85.10	-4.27	1014.45	0.565	Steep	0.85	0.36	0.77	1.22	0.65

[7]. Synthetic schlieren is similar to standard schlieren techniques that use the linear relationship between changes in density and changes in index of refractions to visualize changes in density. However, synthetic schlieren uses a digital camera to track the apparent movement of a randomized dot pattern behind the experiment, which is different from standard schlieren which uses light focused on a knife edge. For this experimental setup, the camera shown in Figure 2b was focused on the mask of random dots behind the experiment. The mask was illuminated by a light box. The jAi Cv-M4+Cl progressive scan camera began recording images after the topography oscillated for 15 periods, which allowed the waves to reach steady state. Images were recorded for three minutes and processed with the commercial software DigiFlow at 6 fps. Digiflow calculates values of $\nabla\rho'/\rho_o$, where ρ' is the perturbations of density. By multiplying these values by $-g$, equation 1 is recovered, although instead of N^2, values for ΔN^2 are generated. An example of the synthetic schlieren results is shown in Figure 3. An outline of the topography has been superimposed over the image in the top left corner. The evanescent waves start at the topography and then moves vertically down towards the turning depth. At the turning depth, the evanescent waves becomes an internal wave and begins to propagate away at an angle. A curved line has been superimposed over the wave to help detail the angle of propagation. This curve was derived from the exponential density profile, and as expected, the internal wave follows the same path. The distance Hr is measured from the bottom of the tank to the turning depth.

With ΔN^2, the kinetic energy of the waves can be estimated using the methods described by Wunsch and Brandt [8]. By assuming that planar wave velocities are multiplied by an amplitude which slowly varies in the z-direction, Wunsch and Brandt related internal wave velocities and ΔN^2 to form the equation

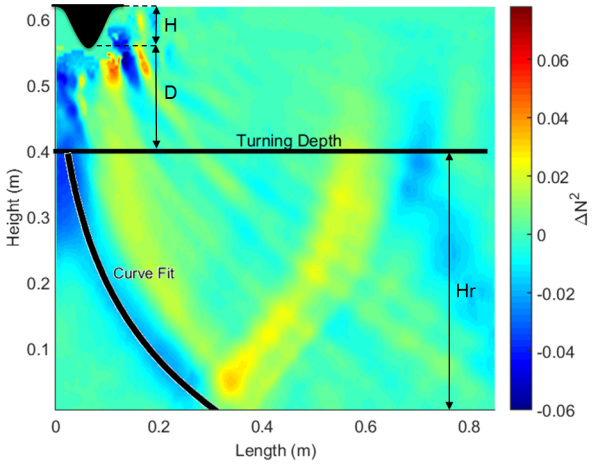

Figure 3: The evanescent wave starts at the tip of the topography, moves vertically downward until it hits the turning depth. Then the evanescent wave becomes a propagating wave and begins to propagate away following a line similar to the curve fit. The color bar shows values of ΔN^2.

$$KE_p = \frac{\omega^2 N^2}{k^2(N^2-\omega^2)+(\omega\partial_z N^2/N^2)}\left|\frac{\Delta N_o^2}{N^2}\right|^2 \tag{4}$$

Here ΔN_o^2 represents the Fourier coefficients of ΔN^2 and k is the horizontal wavenumber. Unfortunately, this equation is not valid in the evanescent region because the horizontal (u) and vertical (v) wave velocities are defined differently between the two types of regions. Instead, the following equations define wave propagation.

$$q^2(z) = k^2(1 - N^2(z)/\omega^2) \tag{5}$$

$$u(x,z,t) = U\exp(-qz)\exp[-i(kx-\omega t)] \tag{6}$$

$$w(x,z,t) = W\exp(-qz)\exp[-i(kx-\omega t)] \tag{7}$$

$$\Delta N^2(z) = \Delta N_o^2\exp(-qz)\exp[-i(kx-\omega t)] \tag{8}$$

Following the methods outlined by Wunsch

and Brandt to derive (4), we find that kinetic energy in the evanescent region can be estimated by

$$KE_e = \left| \frac{q\omega\Delta N_o^2}{k(\omega\partial_z N^2 + qN^2)} \right|^2 + \left| \frac{i\omega\Delta N_o^2}{\omega\partial_z N^2 + qN^2} \right|^2 \quad (9)$$

It should be noted that $m_1 = iq$, which accounts for the decaying wave. Thus while q is real and is used throughout this paper, the vertical wavenumber in the evanescent region, m_1, is imaginary.

3 Results

To compare each of the cases, the calculated kinetic energy was normalized by the kinetic energy at the tip of the topography. This value is denoted as $KE_{e,m}$. The normalized energy is then $KE^* = KE/KE_{e,m}$. Similarly, the height was normalized as $z^* = (z - z_{td})/z_{td}$. Thus $z^* = 0$ at the turning depth, is positive in the evanescent region, and negative in the propagating region.

The kinetic energy of the evanescent and internal waves was calculated for each test case. An example comparing two cases is shown in Figure 4. The blue line is Case 12 and the red line is Case 14. The highest kinetic energy is seen at the top of the graph, where the evanescent wave starts and moves down towards the turning depth. A general decrease in kinetic energy is seen in this region, as would be expected for decaying, evanescent waves. At the turning depth ($z^* = 0$), the evanescent waves become propagating internal waves. It is expected that the normalized kinetic energy would be constant in this area. Case 12 shows a slight increase in kinetic energy in the propagating region, while Case 14 indicates an oscillating kinetic energy with a slight decrease. However, the changes in kinetic energy in the propagating region for both cases are much smaller than the changes in the evanescent region.

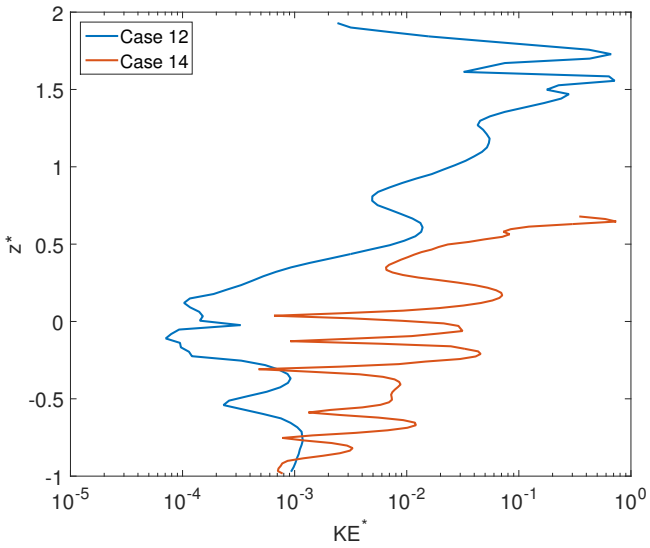

Figure 4: A comparison of Case 12 and Case 14 which have the same topography. The overall higher kinetic energy for Case 14 is due to a higher H/D and a lower Fr_{evan}.

The two cases have the same value of Fr_{prop}, but Case 14 has a higher H/D and a lower Fr_{evan}. The increase in H/D indicates that the topography is closer to the turning depth in Case 14, and thus the evanescent wave did not decay as much because it traveled a shorter distance. A higher Fr_{evan} indicates a weak stratification, and thus the evanescent wave would decay more quickly. Case 12 has a higher Fr_{evan} and a lower kinetic energy in both the propagating and evanescent region than Case 14.

A full comparison of each test case is presented in Figure 5. Each data point corresponds to the average kinetic energy throughout the propagating region, normalized by $KE_{e,m}$. Notice that trends seen in Figure 4 are still clear, though more trends are now visible. In Figure 5a, decreasing Fr_{evan} increases kinetic energy, and there is a very similar trend for both the Medium and Steep topography, although there is a large spread for KE^* at Fr_{evan} near 1.1. This may be an indication that there is a limit on the im-

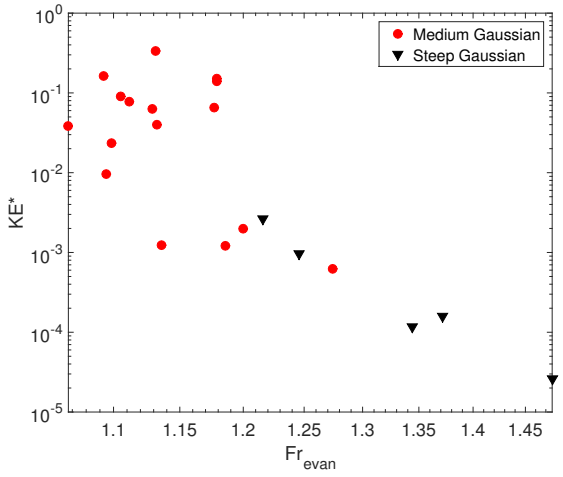

(a) Fr_{evan} vs KE^*

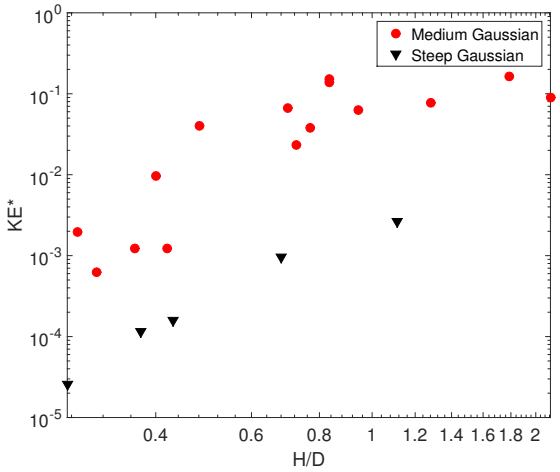

(b) H/D vs KE^*

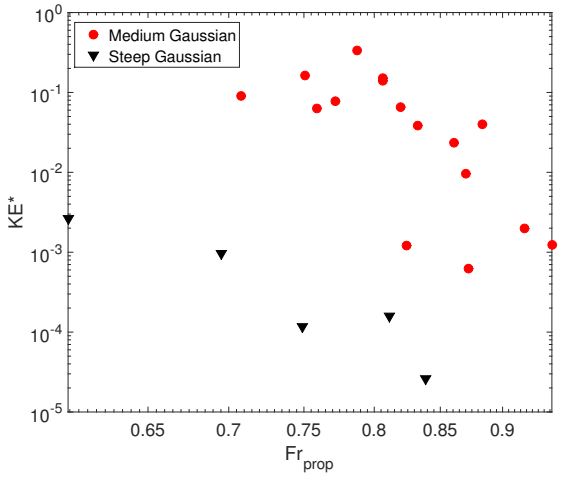

(c) Fr_{prop} vs KE^*

Figure 5: Each figure compares the average, normalized kinetic energy (KE^*) in the propagating region for the 23 cases shown in Table 1. The black triangles represent the Steep Gaussian, while the red circles represent the Medium Gaussian. Each axis is on a log-log scale.

pact of the Fr_{evan}. Further testing would be needed to see if this grouping occurs also for the Steep topography.

In Figure 5b, there is a separation between the Medium and Steep topographies. While they follow similar slopes, two separate trend lines might be needed to describe each topography. It is possible that these differences are due to the variation in the Froude numbers for each point. As H/D increases, the topography comes closer to the turning depth, and it is expected that the normalized kinetic energy will eventually asymptote towards 1 as there would be no loss of kinetic energy through the evanescent region. This is because the topography is so close to the turning depth that there is no longer an evanescent region. While the data seems to indicate a leveling off of the increase of kinetic energy, further testing at higher H/D values would be required.

Figure 5c indicates that increasing Fr_{prop} decreases the kinetic energy of the propagating waves, and that there are separate but similar trends for each topography. While the affects of Fr_{evan} seem to decrease for values approaching 1, this trend is not seen in Fr_{prop}. The overall trend of decreasing relative kinetic energy was not expected. Based on Eq 4, it was assumed that as Fr_{prop} increases, the overall kinetic energy would also increase. Further exploration of this parameter is needed to fully understand this difference.

All of the data indicates that for the same non-dimensional values, the medium topography has more relative kinetic energy than the steep topography. However, there needs to be further testing done to increase the overlap of each non-dimensional parameter for the two topographies. Also, while the individual trends of each parameter was shown here, it is possible that there is an interdependence of Fr_{evan}, Fr_{prop}, and H/D; combinations of these parameters compared to kinetic energy may provide further insight on how a turning depth affects the kinetic energy of propagating internal waves, as well as give understanding to the unusual trend seen with Fr_{prop}.

4 Conclusions

Internal waves generated by evanescent waves passing through a turning depth are affected by the shape of the topography, the Froude number and the distance from the topography to the turning depth. By increasing W/H from 0.45 to 1.8, the kinetic energy of the internal waves always increased, regardless of the other factors.

Future work includes a comparison of experiments to linear theory accounting for the variation in natural frequency. This model will then allow the estimation of kinetic energy of internal waves generated from evanescent waves formed in the ocean.

Acknowledgments

Funding for this project has been provided by the Utah NASA Space Grant Consortium, Brigham Young University Department of Graduate Studies, and NSF Grant #1606040.

The authors would also like to acknowledge the support of Katie Pusey, Alicia Oliphant, Jason Porter, Kyle Hakes, and Amy Briggs, the undergraduate research assistants in the Stratified Flow Lab at Brigham Young University.

References

[1] C. J. Nappo, *An introduction to atmospheric gravity waves.* San Diego, California: Academic Press, 2002.

[2] B. R. Sutherland, *Internal Gravity Waves.* Cambridge, United Kingdom: Cambridge University Press, 2010.

[3] B. King, M. Stone, H. P. Zhang, T. Gerkema, M. Marder, R. B. Scott, and H. L. Swinney, "Buoyancy frequency profiles and internal semidiurnal tide turning depths in the oceans," *Journal of Geophysical Research: Oceans*, vol. 117, no. C4, 2012.

[4] M. S. Paoletti and H. L. Swinney, "Propagating and evanescent internal waves in a deep ocean model," *Journal of Fluid Mechanics*, vol. 706, pp. 571–583, Sep 2012.

[5] J. Lighthill, *Waves in fluids*. Cambridge University Press, 1978.

[6] D. F. Hill, "General density gradients in general domains: the two-tank method revisited," *Experiments in Fluids*, vol. 32, no. 4, 2002.

[7] S. B. Dalziel, G. O. Hughes, and B. R. Sutherland, "Whole-field density measurements by 'synthetic schlieren'," *Experiments in Fluids*, vol. 28, no. 4, pp. 322–335, 04/01 2000.

[8] S. Wunsch and A. Brandt, "Laboratory experiments on internal wave interactions with a pycnocline," *Expts. in Fluids*, vol. 53, pp. 1663–1679, 2012.